

www.acsami.org Research Article

# Resonant Degenerate Four-Wave Mixing at the Defect Energy Levels of 2D Organic-Inorganic Hybrid Perovskite Crystals

Brian A. Ko, Keith Berry, Zhaojun Qin, Alexei V. Sokolov, Jonathan Hu, Marlan O. Scully, Jiming Bao, and Zhenrong Zhang\*



Cite This: https://doi.org/10.1021/acsami.1c14092



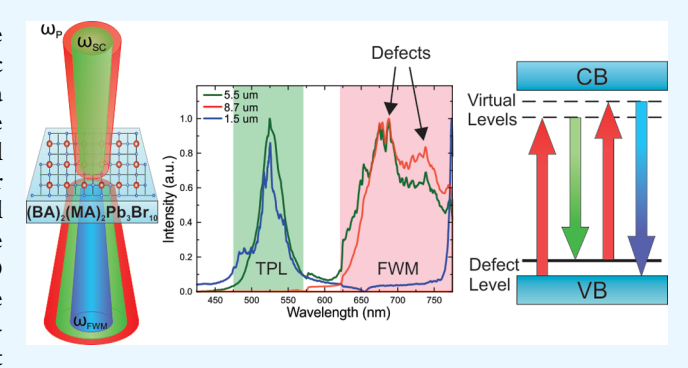
**ACCESS** 

III Metrics & More

Article Recommendations

Supporting Information

ABSTRACT: Two-dimensional organic—inorganic lead halide perovskites are generating great interest due to their optoelectronic characteristics such as high solar energy conversion efficiency and a tunable direct band gap in the visible regime. However, the presence of defect states within the two-dimensional crystal structure can affect these properties, resulting in changes to their band gap emission as well as the emergence of nonlinear optical phenomena. Here, we have investigated the effects of the presence of defect states on the nonlinear optical phenomena of the 2D hybrid perovskite  $(\mathrm{BA})_2(\mathrm{MA})_2\mathrm{Pb}_3\mathrm{Br}_{10}.$  When two pulses, one narrowband pump pulse centered at 800 nm and one supercontinuum pulse with bandwidth from 800—1100 nm, are incident



on a perovskite flake, degenerate four-wave mixing (FWM) occurs, with peaks corresponding to the energy levels of the defect states present within the crystal. The longer carrier lifetime of the defect state, in comparison to that of virtual transitions that take place in nonresonant FWM processes, allows for a larger population of electrons to be excited by the second pump photon, resulting in increased FWM signal at the defect energy levels. The quenching of the two-photon luminescence as flake thickness increases is also observed and attributed to the increased presence of defects within the flake at larger thicknesses. This technique shows the potential of detecting defect energy levels in crystals using FWM for a variety of optoelectronic applications.

KEYWORDS: perovskites, nonlinear Optics, materials, defects, fluorescence

# ■ INTRODUCTION

Organic-inorganic lead halide perovskites are semiconductors that have seen a great increase in interest due to their optoelectronic characteristics. 1-8 Three-dimensional perovskites have been shown to have high energy efficiencies, as high as 20% in the case of heterojunction solar cells using an iodide-bromide hybrid perovskite  $(MA)Pb(I_{1-x}Br_x)_3^9$  In addition to high efficiencies, the ease of synthesis has made them promising candidates in photovoltaic (PV) applications. 10,11 However, 3D lead halide perovskites suffer from stability issues, such as high thermal damage potential under irradiation 12,13 and decomposition while exposed to water vapor. 14,15 Two-dimensional Ruddlesden-Popper hybrid perovskites utilizing a combination of layered 3D perovskites separated by organic cations have been proposed due to increased stability in comparison to 3D perovskites while still maintaining good conversion efficiencies. 16 This increased stability coupled with their band gaps, which are tunable in the visible regime by changing the doping concentration, has led to their use as fluorescent materials due to their high photoluminescent quantum yield<sup>17</sup> either as microlasers<sup>2,18</sup> or diodes. 19-23 As nonlinear optical phenomena form the basis of many modern technologies, 2D hybrid organic-inorganic

perovskites have seen an increase in study for their potential in this field.<sup>24</sup> Maczka et al. observed second-harmonic generation, third-harmonic generation (THG), and multiphoton luminescence from methylhydrazinium lead bromide.<sup>25</sup> Chen et al. studied the nonlinear optical properties of three different 2D hybrid perovskites using third-harmonic generation to determine that their responses are dependent on their crystal structures.<sup>26</sup> 2D hybrid perovskites have also been shown to exhibit a maximum THG conversion efficiency of 0.006%, which is five orders of magnitude greater than other 2D materials.<sup>27</sup> Johnson et al. were able to measure the thirdorder nonlinear susceptibility of methylammonium lead halide films on the order of  $1.6 \times 10^{-6}$  esu, which is comparable to other materials, highlighting perovskites as a potential candidate for optoelectronic applications.<sup>28</sup> The acceleration in research interest in organometallic lead halides has led to

Received: July 25, 2021 Accepted: November 9, 2021



additional novel uses of the material, such as humidity sensing<sup>29</sup> and NH<sub>3</sub> gas detection.<sup>5</sup> However, these samples are prone to defects in their crystal structure, affecting their energy efficiency by introducing nonradiative recombination pathways.11

Defects within a crystal structure are abnormalities in the regular structure. Intrinsic defects can take on the form as simple atomic vacancies or interstitials or as more complex antisites (two atoms switch locations). 30-33 Extrinsic defects can come in the form of doping the crystal, substituting one atom with that of the dopant. 34-38 Both of these types of defects cause changes to the density of states (DOS) of the crystal, fundamentally changing the band structure and subsequent emission properties. 5,6,10,11,31,39-46 Defects within the crystal structure of organometallic perovskites can lead to a variety of phenomena, including the introduction of nonradiative recombination pathways for the electron-hole pairs to decay into, leading to a quenching of the characteristic band gap emission.<sup>6</sup> In the photovoltaic industry, these phenomena are a hindrance to the conversion efficiency of the PV cell. In other applications, the formation of defect energy levels can lead to its use as an emitter. 10,23,35,40,47,48 Defect levels have longer lifetimes, on the order of nanoseconds, 49-52 than that of virtual levels, allowing for the enhancement of nonlinear optical phenomena such as four-wave mixing (FWM). FWM in semiconductors has been well established to study lightmatter interaction and the coupling between electronic states that occur within the crystal such as the excitonic coherence of GaN, <sup>53</sup> the dynamics of excitonic broadening in perovskites, <sup>54,55</sup> and our previous work on FWM at the excitonic resonance of MoS<sub>2</sub>. <sup>56</sup> FWM processes are attractive techniques due to decreased linear absorption, as the wavelengths typically used in FWM experiments are of lower energy than the band gap of the material. However, nonresonant four-wave mixing (NR-FWM) can disturb and overpower the resonant signal. The NR-FWM signal arises due to excitation of electrons into short-lived (<1 ps) virtual states, <sup>57,58</sup> which then are further excited by another pump photon to be emitted as an anti-Stokes signal. The presence of defects allows for coherent excitation of electrons into the defect levels so it is no longer nonresonant but instead reveals the property of the material.

Current experimental methods of optical detection of the defects present within a crystal are limited to mainly lowtemperature studies, such as those done on CdTe<sup>59</sup> and MoS<sub>2</sub><sup>60</sup> as well as perovskite materials, 6,8 or photoemission studies, such as angle-resolved photoemission spectroscopy (ARPES), which requires ultrahigh-vacuum (UHV) conditions. Previous FWM experiments on perovskites have shown that weak exciton-carrier interactions prevents the enhancement of excitonic FWM signals that are tied to excitationinduced dephasing.<sup>55</sup> Other FWM experiments on perovskites have shown that below-band gap excitation leads to spectral broadening of the excitonic emission due to an increased number of inter- and intraband FWM combinations that can contribute to the emission.<sup>61</sup> However, the correlation of the defect states in perovskites with their nonlinear optical phenomena has not been reported.

In this experiment, two incident pulses—one narrowband pump pulse centered at 800 nm and a broadband supercontinuum pulse from 800-1100 nm-are utilized to study the nonlinear optical properties of flakes consisting of the organometallic perovskite butylammonium methylammonium lead bromide (BA)<sub>2</sub>(MA)<sub>2</sub>Pb<sub>3</sub>Br<sub>10</sub> (Figure 1). By coherently

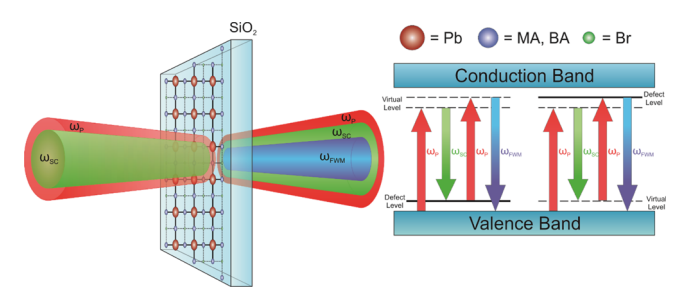


Figure 1. Degenerate four-wave mixing at the defect energy levels of a (MA)<sub>2</sub>(BA)<sub>2</sub>Pb<sub>3</sub>Br<sub>10</sub>. Two photons of the pump pulse and one photon of the supercontinuum pulse interact to produce a fourth pulse. In the presence of defect levels, the beat frequency of the two pulses  $(\omega_P - \omega_{SC})$  can be resonant with the energy level of a trap state or the FWM relation  $2\omega_{\rm P}-\omega_{\rm SC}$  is equal to the energy of a donor state, resulting in increased emission at that energy.

exciting carriers into the defect states in our experiment, defect state detection can be performed in ambient conditions as a larger population of charge carriers is excited. Furthermore, the use of a supercontinuum pulse allows for simultaneous measurement of multiple defect levels via FWM as the broadband nature allows for multiple defect levels to be resonantly filled. When the two pulses are temporally and spatially overlapped, degenerate FWM occurs. The resultant FWM signal increases with sample thickness due to the increased presence of defect sites within the optical path. These defect states enhance the FWM emission by providing a longer carrier lifetime than virtual electronic transitions.

# **■ EXPERIMENTAL SECTION**

Butylammonium methylammonium lead bromide, (BA)<sub>2</sub>(MA)<sub>2</sub>Pb<sub>3</sub>Br<sub>10</sub>, crystals were synthesized by dissolving the precursors PbO (0.59 mmol, 131.7 mg, Sigma-Aldrich), BABr (0.19 mmol, 29.3 mg, Sigma-Aldrich), and MABr (0.4 mmol, 44.8 mg, Greatcell Solar) in an acid mixture consisting of 0.9 mL of HBr (Sigma-Aldrich) and 0.1 mL of H<sub>3</sub>PO<sub>2</sub> (Sigma-Aldrich) in a 10 mL glass vial. Using a magnetic stir rod, the vial was heated to 393 K in an oil bath.<sup>23</sup> After the precursors are completely dissolved and the solution becomes transparent, the stirring is stopped and the solution was cooled at a rate of 2 K/min, during which crystals are formed. The crystals are collected via filtration, and the residual solvent was removed via a vacuum pump. X-ray diffraction (XRD) measurements were taken on the flake to determine that the crystal structure agreed with previous synthesis attempts and XRD measurements taken by Li et al.<sup>7</sup> These are shown in Table S1.

(BA)<sub>2</sub>(MA)<sub>2</sub>Pb<sub>3</sub>Br<sub>10</sub> flake samples were prepared by mechanical exfoliation method with adhesive tape on the as-synthesized crystals and deposited onto a glass slide. To create a substrate capable of observing the perovskite flake using a scanning electron microscope (SEM) while also allowing for four-wave mixing optical transmission measurements, a thin layer of indium tin oxide was deposited via RF magnetron sputtering (K-Lab ITO target, 50 W, 45 s deposition time, 5.0 mTorr process pressure) prior to application of the perovskite flake. The flake shown in Figures 2 and 4, as well as its satellite flakes, were studied in order to observe the interaction of the two incident pulses with perovskite flakes of different thicknesses. SEM revealed that the flake was macroscopically flat outside of step edges. To determine the thickness of the perovskite flake, a 3D laser scanning microscope (3D-LSM) was utilized (Olympus LEXT OLS5000). The 3D-LSM map (Figure 2b) showed that the large flake and its surrounding satellite flakes are divided into three distinct categories (Figure 2c)—the majority of the large flake measuring approximately  $8-9 \mu m$  in thickness (red region), a small region of the large flake measuring between 5.0 and 7.0  $\mu$ m in thickness (green region), and the thin satellite flakes measuring approximately 1.3  $\mu$ m (blue region).

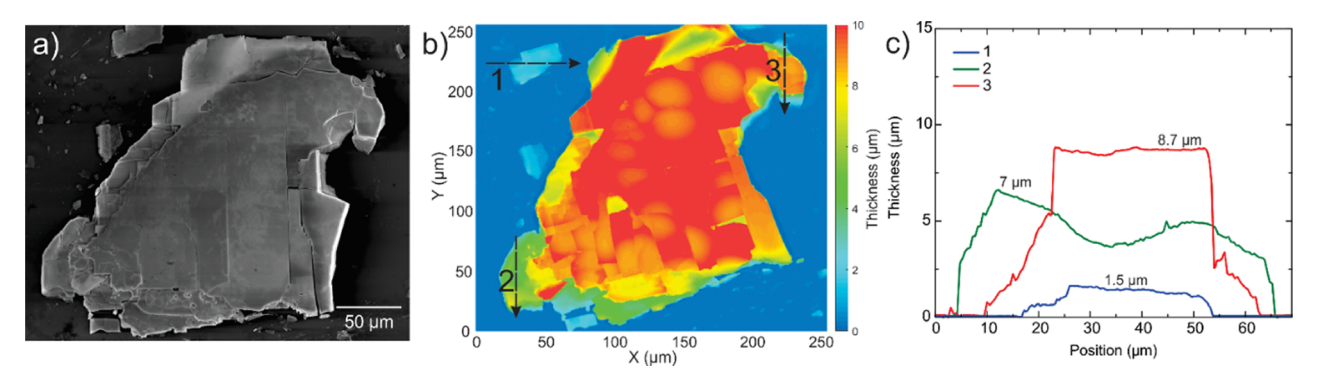


Figure 2. (a) Scanning electron microscope (SEM) image of representative  $(BA)_2(MA)_2Pb_3Br_{10}$  flake. (b) 3D laser-scanning microscope image of representative flake, showing the thickness of the flake. (c) Cross section of the flake along the arrows drawn in (b).

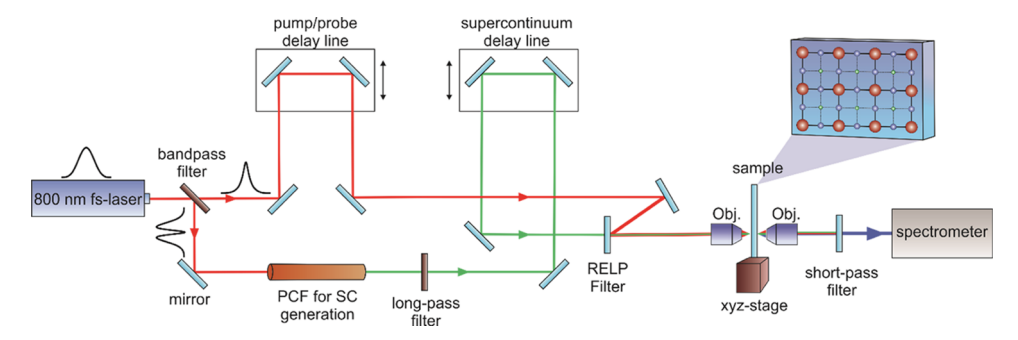


Figure 3. Experimental setup. A femtosecond laser (800 nm, 100 fs, 30 nm FWHM) is split into two pulses using a band-pass filter. The narrow, transmitted pulse supplied the 800 nm pulse, while the reflected light pumps a photonic crystal fiber to create the broadband supercontinuum pulse.

These regions are denoted by red, green, and blue dots in Figure 4a. Electron diffraction spectroscopy (EDS) measurements were taken using an SEM (Figure 2a) to determine whether there are any compositional differences between the regions (see Figure S1). The EDS measurements revealed that the flake has uniform composition throughout. Confocal laser-scanning microscopy (CLSM; Olympus FV-3000) was performed using an excitation wavelength of 405 nm in order to observe the photoluminescence emission of the perovskite flake.

The optical measurements were performed using a multiplex coherent anti-Stokes Raman spectroscopy<sup>56</sup> (CARS) setup (CARS-KT, Newport Optics) as shown in Figure 3. In the CARS setup, an Nd:YAG laser (Millenia eV) pumped a Ti:Sapphire oscillator (Tsunami, Spectra Physics) to produce femtosecond laser pulses (~100 fs pulse duration, 80 MHz repetition rate). The oscillator was mode-locked to produce pulses with a 30 nm bandwidth full width at half maximum centered at approximately 800 nm. The pulse train was then split using a band-pass filter to create two pulse trains—one narrowband (3 nm FWHM) pulse that acts as the pump/probe pulse and the remaining oscillator pulse. The remaining oscillator pulse was then directed into a photonic crystal fiber (PCF-800) to generate a broadband supercontinuum. A linear polarizer was placed in each of the pulse trains to optimize their polarizations for maximum FWM signal. The two pulse trains were recombined at a razor-edge longpass (RELP) filter centered at 800 nm and directed via mirrors to the sample. A neutral-density filter is placed just after the RELP to attenuate the incident pulses without changing their spectral character to prevent excessive thermal damage to the sample during measurement. The incident beams were removed after the sample using two short-pass filters, and the resultant spectrum is collected using a spectrometer (Horiba iHR 550). The pulse powers for the pump and SC pulses used in this experiment were 3.7 and 10.3 mW, respectively. For pulse power dependence measurements, a variable neutral-density filter was placed in one of the pulse trains before the RELP to attenuate the pulse.

## RESULTS

Two-photon luminescence (TPL) and FWM spectra were obtained at three locations on the perovskite flake and its surrounding flakes (see Figure 4a) corresponding to three distinct regions as shown in Figure 2b. The representative spectra shown in Figure 4b are characterized by two separate phenomena—a green emission centered at approximately 525 nm with a shoulder at 485 nm and a red emission starting from approximately 650 nm until the cutoff from the short-pass filters (785 nm) that block the incident pulses. The green 525 nm emission is TPL due to two-photon absorption (TPA), 23 and the red 650-785 nm emission is attributed to FWM (see below). The red emission is characterized by many small peaks in the spectra, and the positions of these peaks stay roughly constant as the excitation location is changed. Additional spectra taken at other locations on this flake, as well as locations on other flakes, are shown in Figures S2 and S3, respectively. The optical image of the perovskite flake and its surrounding satellite flakes can be divided into three areas as shown in the LSM image in Figure 2b—one broad area covering the majority of the perovskite sample measuring 8-9 um in thickness (red dot), one small region on the bottom-left corner of the perovskite flake measuring 5–6.4  $\mu$ m in thickness (green dot), and smaller outlying flakes (blue dot) measuring  $0.5-1.5 \mu m$  in thickness—and each area is characterized by the presence of the 525 nm emission, the broad 650 to 785 nm emission, or both. On the majority of the flake (red region in Figure 2b), the red emission spanning from 650 to 785 nm (Figure 4b) is present and much larger than the nearly nonexistent 525 nm emission, while on the thinner satellite flakes (blue region in Figure 2c), only the 525 nm emission is visible with the 650-785 nm emission quenched. Only on the areas with the intermediate thickness (green region in Figure

**ACS Applied Materials & Interfaces** 

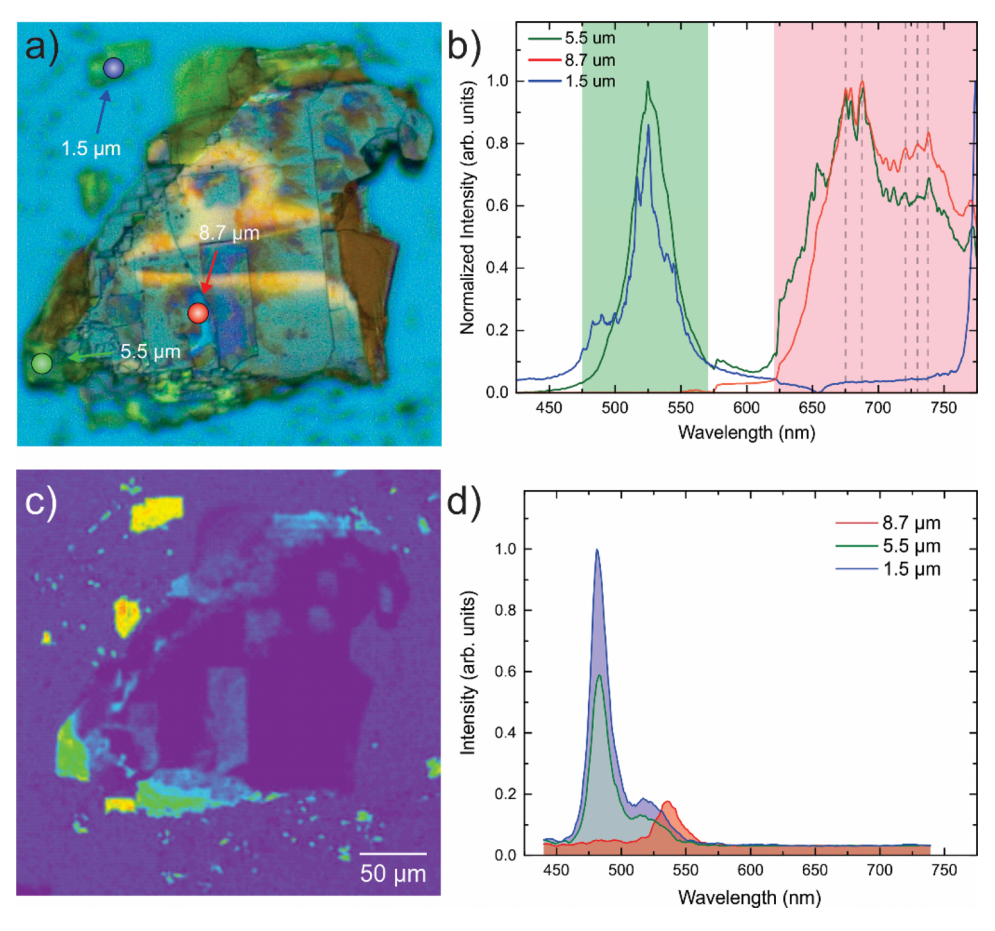


Figure 4. (a) Optical microscope image of the  $(BA)_2(MA)_2Pb_3Br_{10}$  flake. Three different locations with different thicknesses are investigated (red, 8.7  $\mu$ m; green, 5.5  $\mu$ m; blue, 1.5  $\mu$ m). (b) Four-wave mixing (FWM, red region) and two-photon luminescence (TPL) signal (green region) obtained from the locations marked in (a). The TPL signal is visible at the green and blue spots and quenched at the red spot, while the FWM is visible at the red and green spots and quenched at the blue spot. (c) Confocal laser-scanning microscope (CLSM) photoluminescence image (405 nm excitation) of perovskite flake in (a). (d) CLSM spectra at the three locations marked in (a).

2b), occupying a small portion on the bottom left and the upper portion of the large flake in Figure 4a, are both the 525 and 650–785 nm emissions present. Figure 4c,d shows the CLSM (405 nm surface-scanning excitation, 440–740 nm collection) image of the perovskite flake and its surrounding flakes and the photoluminescence (PL) spectra at the three locations depicted in Figure 4a. The CLSM spectra also show a stronger 485 nm peak, which corresponds to the band gap of the 2D hybrid perovskite, than the 525 nm peak corresponding to the edge MAPbBr<sub>3</sub> nanocrystals<sup>23</sup> for the blue and green spots. Similar to the results shown in Figure 4b, the CLSM spectra in Figure 4d shows that the thin satellite flakes exhibit a stronger PL emission than that of the thicker flake.

There has been an extensive debate in the literature regarding the photocarrier dynamics in perovskites that contribute to the quenching of the PL signal. Defects act as traps and affect the diffusion and recombination processes of photocarriers leading to nonradiative losses. <sup>62</sup> It is known that defects and grain boundaries exhibit faster nonradiative decay and are associated with PL quenching. <sup>63</sup> Due to the layered and multigrain structural nature of the perovskite, the defects in these solution-prepared perovskite crystals are not just located at the surface. The thinner the sample, the more uniform the crystals are and the fewer grain boundaries and defects are in the crystal. Therefore, defects in the thicker sample could contribute to the quenching of the PL signal.

Photon reabsorption, or "photon recycling," is another process that reduces the apparent rate of radiative recombination by partially reabsorbing the photons generated by the radiative recombination of the photocarriers (electrons and holes). As the thickness of the perovskite increases, the reabsorption of generated photons increases, which could contribute to the decreases in TPL efficiency. The TPL peak position (525 nm) from edge MAPbBr<sub>3</sub> indicates that the flake has a band gap of 2.39 eV, which agrees with previous reports. As a support of the process of the process of the perovskite increases, which could contribute to the decreases in TPL efficiency. The TPL peak position (525 nm) from edge MAPbBr<sub>3</sub> indicates that the flake has a band gap of 2.39 eV, which agrees with previous reports.

The 3D-LSM scan for sample thickness (Figure 2b) and the FWM/TPA emission seen at the three locations depicted in Figure 4 indicate that FWM signal intensity increases with sample thickness, while the TPL intensity decreases as the thickness increases. On the red spot in Figure 4a, with measured thickness 8.7  $\mu$ m, the FWM/TPL intensity ratio is 555, while on the blue spot (1.5  $\mu$ m), the FWM/TPL ratio is 0.1. On the green spot (thickness 5.5  $\mu$ m), where both FWM and TPL are easily visible, the FWM/TPL intensity ratio is 1.7.

Single pulse excitation experiments were performed to investigate the process behind the green and red emissions. These were performed by simply blocking either of the two pulse trains and measuring the resulting spectra. These are shown in Figure S4. The green spot in Figure 4a was chosen due to the easily visible presence of both the green and red signals. From these measurements, it is evident that the green

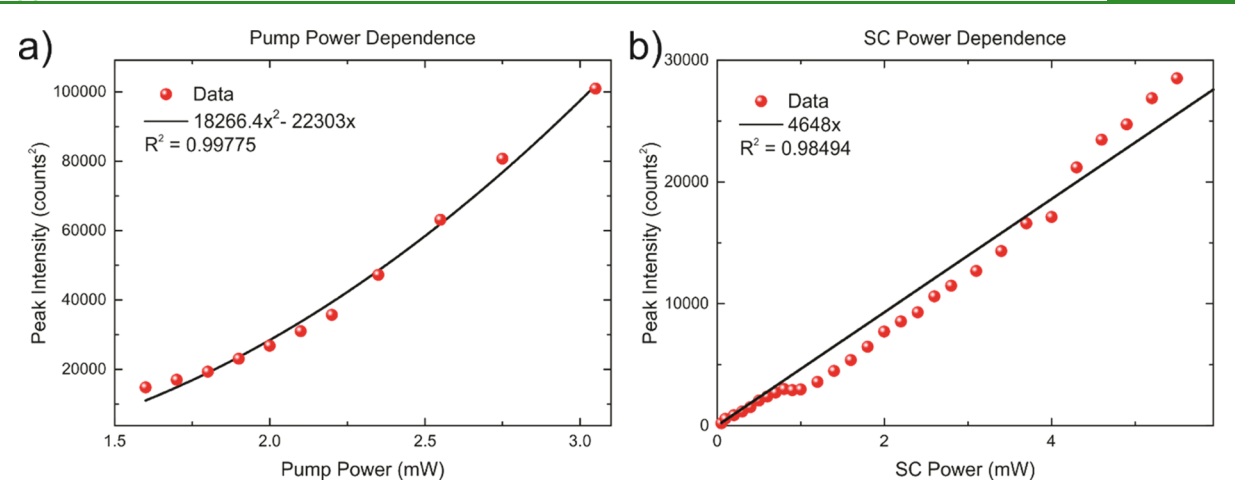


Figure 5. Four-wave mixing (FWM) signal intensity dependence for (a) pump and (b) supercontinuum (SC) pulse energies at the green location of the  $(BA)_2(MA)_2Pb_3Br_{10}$  flake. The quadratic dependence of the FWM signal on the pump power corresponds to the process requiring two pump photons, while the linear dependence on the SC power indicates that a single SC photon is used.

emission observed is TPL as the pump pulse is able to produce the same emission although at a lower intensity. <sup>1,21</sup> The contribution from the supercontinuum pulse to the TPL emission is small. However, the red emission is not observed in either case where one of the two pulse trains are blocked, showing that the red emission is not caused by TPA. With either the pump or the SC only, the red emission is not there (Figure S4).

With both pulse trains required to create the red emission observed in Figure 4b, power dependence measurements were taken to determine the number of photons of each pulse required to make the red emission. In these measurements, the power of one pulse train is kept constant, while the power of the other pulse is modulated using a variable neutral-density filter placed in its path. Temporal and spatial overlap were optimized each time the variable neutral-density filter is modulated to ensure maximum resultant signal. The results of these power dependence measurements are shown in Figure 5. The pump power dependence measurement (Figure 5a) revealed a quadratic dependence of the resultant signal on the pump power, indicating that the process requires two pump photons. On the other hand, modulation of the SC power (Figure 5b) showed a linear power dependence, indicating that a single SC photon is used in the process. The fit for the SC power is not perfectly linear; this is most likely due to the nonlinear nature of four-wave mixing, so linear changes in SC power do not fully translate to linear changes in FWM signal intensity. It can also be attributed to energy from the pump pulse used to pump the PCF that produces the SC that bleeds through and is allowed to continue along the SC path. However, the quadratic component is small. This confirms that the phenomenon creating the red emission is a third-order FWM process.

## DISCUSSION

Based on the 3D-LSM measurements of the perovskite flake thickness (Figure 2a) and the increased FWM to TPL intensity ratio of the red region in Figure 4b, both the TPA and the FWM processes are affected by the thickness of the flake. The quenching of the TPL process as the thickness of the material increases has been previously attributed to the increased presence of defects within the sample. 1,63,68,69 The presence of these defect sites introduces intermediary energy levels

between the valence and conduction bands. As a result, when the incident pulses excite an electron from the valence to the conduction band, the rate of nonradiative recombination into these defect states increases. Thus, the characteristic excitonic emission is quenched for thicker samples. As mentioned above, photon reabsorption could also contribute to the quenching of the TPL signal.

In addition to the quenching of the TPA process, our results show that the increased presence of the defects in thicker perovskite samples can lead to increased FWM signal at these defect energy levels. In NR-FWM, the energy difference  $\omega_{\rm p}$  –  $\omega_{\rm s}$  corresponds to a virtual state; the lifetime of these virtual states is much shorter than that of a vibrational mode (i.e., Raman) or an excitonic resonance (i.e., TPA) that is intrinsic to the sample, whereas the relative lifetime of photoluminescence produced by a defect state is on the order of nanoseconds. 49-52 In contrast, the lifetime of a virtual state during NR-FWM generally falls on the order of picoseconds.<sup>58</sup> In a thin sample, the presence of a defect site within the laser path is low. As a result, the efficiency of the FWM process at defect peak locations within a thin organometallic perovskite flake is low. However, as the thickness and the number of defects present within the illuminated portion of the sample increases, the frequency difference between the pump and SC pulses becomes resonant with one of the defect states, resulting in a longer-lived excitation. Therefore, the FWM process is enhanced as more charge carriers are available at the defect energy level (Figure 1) within the optical path. In the presence of a defect energy level, either the energy difference between the pump and SC photons  $\omega_p - \omega_s$  or the sum frequency  $2\omega_p$  $-\omega_{\rm s}$  is resonant with the trap state. The extended lifetime of the defect levels allows for further interaction with an additional photon, resulting in FWM peaks at the defect energy levels. Furthermore, as the SC pulse is a broadband pulse, multiple defect energy levels can be excited, allowing for the determination of multiple defect states with a single measurement as evidenced by the multiple peaks in the red emission seen in the red region of Figure 2b.

Thin film interference, where internal reflections within the flake can cause variations in the spectrum of the SC pulse, was ruled out by comparing the overall shape of the FWM spectra obtained at different locations on the flake but within the same thickness regime. In thin film interference, the layered

structure of the perovskite flake can make the flake be viewed as multiple flakes of intermediate size stacked together, which would cause varying interference rates depending on the wavelength of the SC pulse. These interference effects would then cause large shifts in the shape of the overall resultant spectra even through small translations of the focal point on the flake. However, on examination of the resultant spectra shown in Figure 4b and Figure S2b on the red region with thicknesses of  $8-9 \mu m$  in Figure 2a, the peak locations within the FWM region stay constant while the underlying background changes drastically. This rules out the possibility that the peaks in the FWM signal are caused by nonresonant FWM due to thin film interference, and instead, the FWM signal is dependent on the intrinsic characteristics of the perovskite flake.

The binding energy of the defect levels present in the sample can be simply derived by calculating the difference in energy between the incident pump pulse (800 nm, 1.55 eV) and the resultant emission spectrum. From the spectra obtained in the red region of Figure 2, the observed peaks are shown to be located at 675 (1.84 eV), 690 (1.80 eV), 720 (1.72 eV), 730 (1.70 eV), and 740 (1.68 eV) nm. In the proposed FWM scheme, the energy values of these defect states would be 0.29, 0.25, 0.17, 0.15, and 0.13 eV above the valence band or below the conduction band as FWM measures the energy difference. Various donor and acceptor defect levels have been calculated through DFT calculations on the band structure of the perovskite with the presence of defects. 30,32,33 Based on previous DFT calculations of MAPbBr<sub>3</sub> conducted by Mannodi-Kanakkithodi et al., Shi et al., and Motti et al., the defect energy levels observed in this experiment would correspond to deep defects located in the band between the valence and conduction bands. 30,32,33 Table 1 lists the possible

Table 1. Measured Defect State Energies and Possible Defects in (BA)<sub>2</sub>(MA)<sub>2</sub>Pb<sub>3</sub>Br<sub>10</sub>

Wavelength	Measured Energy	Possible Defect Source
675 nm	0.29 eV	$Br_i(+/-)$ , <sup>32</sup> $Pb_i(+/2+)$ , <sup>33</sup> $Pb_{MA}(+/0)$ <sup>30</sup>
690 nm	0.25 eV	$V_{Pb}(0/2-)$ , 32 $V_{Pb}(-/2-)$ 30
720 nm	0.17 eV	$V_{Pb}(-/2-)^{32}$
730 nm	0.15 eV	$Br_{MA}(0/-)$ , 33 $V_{Br}(0/-)$ 32
740 nm	0.13 eV	$V_{MA}(0/-)$ , 30,33 $Br_i(0/-)$ 32

defects within the crystal structure that would create these calculated defect levels. Of these potential defects, the most stable in terms of formation energy are written in bold. Because the energy values correspond so closely to those calculated by previous DFT calculations, the defects seen are most likely attributed to defects in the MAPbBr3 structure instead of the more stable BAPbBr<sub>3</sub> structure.

The peaks observed at the defect energy levels in the FWM spectra can possibly be attributed to Fabry-Perot resonance due to the layered nature of the perovskite flake. However, due to the fact that spacing between Fabry-Perot peaks scales with the thickness of the material, the spacing between peaks within the FWM regime in Figure 4b would vary by up to 58% instead of staying constant as was observed (see the Supporting Information). However, our results show the spacing is between the observed peaks is nearly identical between the red and green locations, showing that these peaks are resultant from an intrinsic property of the material (i.e., defects in crystal structure) instead of macroscopic geometric sources.

Dark excitonic transitions describe excitonic transitions that are spatially direct but normally optically forbidden due to a required spin state transition or momentum transfer. They are a possible source of the peaks in the FWM signal. These dark excitonic transitions are strongly coupled to the optically allowed transitions, allowing them to be observed via FWM schemes. For example, Tollerud et al. were able to characterize dark excitons within the InGaAs/GaAs quantum wells using a coherent multidimensional spectroscopy (CMDS), a type of FWM spectroscopy.<sup>70</sup> However, CMDS generally utilizes three separate pulses in order to vary the time delays between the first and second pulses as well as the delay between the second and third pulses. As our experimental setup utilizes a degenerate four-wave mixing scheme with only two separate pulses, it is unlikely that our FWM results are correlated to the dark excitons.

The defects within the crystals could have been formed either during synthesis or the experimental procedure. Solution-processed hybrid perovskites are known to exhibit heterogeneity among the grains. 62,63 Lead halide perovskites have been found to be susceptible to thermal damage over time. 11,12,71-73 2D hybrid perovskites have also been found to degrade back to the 3D perovskite, which can lead to trapped states.<sup>23</sup> Perovskites are also sensitive to humidity in the surrounding environment, which can further lead to defect formation. 14,15,74

This method, to our knowledge, is the first to correlate the defect energy levels with the FWM signal produced. This method is capable of measuring the defect levels of a bulk semiconductor while avoiding the high linear absorption that comes with the increased layer count. FWM processes generally scale with sample thickness, making it more suitable for analysis of bulk crystals. Also, by utilizing two laser pulses, both with photon energies lower than the characteristic band gap energy, the induced photoluminescence at the bandgap that can disturb nearby defect level measurements is separated from the FWM emission created by the defect levels. Previously, defect level measurement using laser pulses was limited to low-temperature studies such as those performed by Zázvorka et al. on CdTe<sup>59</sup> and by Guo et al. and Zhang et al. on perovskites.<sup>6,8</sup> This method can obtain the defect levels at room temperature by coherently exciting molecules into the defect state and obtaining the defect levels before thermal excitation of the electrons out of the defect states can occur. 59

# CONCLUSIONS

The relation between the thickness of an organometallic perovskite flake, the increased number of defects within the flake, and the ratio between the TPL and FWM signal intensities are measured using temporal and spatially-overlapped pulses—one narrowband pulse at 800 nm and one broadband SC pulse with wavelength 800-1100 nm. As the thickness of the flake increases, the TPA process is inhibited by the increased number of defect states within the flake that allow for nonradiative recombination of electron-hole pairs that are excited by the incident pulses. However, the increased number of defects creates real energy levels that are resonant with the pump-SC energy difference  $\omega_p - \omega_s$ , resulting in longer-lived states. The longer carrier lifetimes result in an increased number of electrons in these decay states, resulting in an increased FWM signal as the thickness of the flake increases. This FWM scheme can be used to identify defect energy levels within a semiconductor by using two pulses that

are of lower energy than the characteristic band gap, resulting in lower thermal absorption and, thus, thermal decomposition of the sample.

## ASSOCIATED CONTENT

# Supporting Information

The Supporting Information is available free of charge at https://pubs.acs.org/doi/10.1021/acsami.1c14092.

X-ray diffraction data from the perovskite flake; energy-dispersive spectroscopy of the perovskite flake, along with the calculated elemental composition of the flake; TPL and FWM measurements on additional locations on the perovskite flake, as well as an additional perovskite flake; single-pulse measurements on the perovskite flake; discussion on Fabry–Perot resonance (PDF)

#### AUTHOR INFORMATION

# **Corresponding Author**

Zhenrong Zhang — Baylor University, Waco, Texas 76706, United States; ⊚ orcid.org/0000-0003-3969-2326; Email: Zhenrong Zhang@baylor.edu

#### Authors

Brian A. Ko — Baylor University, Waco, Texas 76706, United States; Texas A&M University, College Station, Texas 77843, United States; Occid.org/0000-0003-3520-3484

Keith Berry – Baylor University, Waco, Texas 76706, United States

**Zhaojun Qin** – University of Houston, Houston, Texas 77004, United States

Alexei V. Sokolov — Baylor University, Waco, Texas 76706, United States; Texas A&M University, College Station, Texas 77843, United States

Jonathan Hu — Baylor University, Waco, Texas 76706, United States; orcid.org/0000-0001-6426-3051

Marlan O. Scully – Baylor University, Waco, Texas 76706, United States; Texas A&M University, College Station, Texas 77843, United States; Princeton University, Princeton, New Jersey 08544, United States

Jiming Bao − University of Houston, Houston, Texas 77004, United States; orcid.org/0000-0002-6819-0117

Complete contact information is available at: https://pubs.acs.org/10.1021/acsami.1c14092

## **Author Contributions**

Z.Z. and J.B. designed and conceived the project. Z.Q. synthesized samples. B.A.K. performed measurements, analyzed data, and drafted the paper. K.B. worked on analysis of the CLSM and FWM results. M.O.S., Z.Z., and J.H. supervised the project. All authors discussed the results and commented on the manuscript.

## Funding

K.B., Z.Z., and J.H. are supported by the Baylor OVPR Postdoctoral Fellowship Award. M.O.S. acknowledges support from the Robert A. Welch Foundation (grant A-1547). J.B. acknowledges support from the Robert A. Welch Foundation (grant E-1728). Z.Z. acknowledges support from the National Science Foundation under grant CHE-1905043.

### Notes

The authors declare no competing financial interest.

## ACKNOWLEDGMENTS

The authors would like to thank the Center for Microscopy and Imaging at Baylor University for use of their facility as well as the Olympus Corporation for use of their 3D laser-scanning microscope.

# REFERENCES

- (1) Liu, W.; Xing, J.; Zhao, J.; Wen, X.; Wang, K.; Lu, P.; Xiong, Q. Giant Two-Photon Absorption and Its Saturation in 2D Organic-Inorganic Perovskite. *Advanced Optical Materials* **2017**, *5*, 1601045.
- (2) Li, P.; Chen, Y.; Yang, T.; Wang, Z.; Lin, H.; Xu, Y.; Li, L.; Mu, H.; Shivananju, B. N.; Zhang, Y.; Zhang, Q.; Pan, A.; Li, S.; Tang, D.; Jia, B.; Zhang, H.; Bao, Q. Two-Dimensional CH<sub>3</sub>NH<sub>3</sub>PbI<sub>3</sub> Perovskite Nanosheets for Ultrafast Pulsed Fiber Lasers. *ACS Appl. Mater. Interfaces* **2017**, *9*, 12759–12765.
- (3) Buin, A.; Comin, R.; Xu, J.; Ip, A. H.; Sargent, E. H. Halide-Dependent Electronic Structure of Organolead Perovskite Materials. *Chem. Mater.* **2015**, *27*, 4405–4412.
- (4) Wu, K.; Bera, A.; Ma, C.; Du, Y.; Yang, Y.; Li, L.; Wu, T. Temperature-dependent Excitonic Photoluminescence of Hybrid Organometal Halide Perovskite Films. *Phys. Chem. Chem. Phys.* **2014**, *16*, 22476–22481.
- (5) Li, G.; Zhang, W.; She, C.; Jia, S.; Liu, S.; Yue, F.; Jing, C.; Cheng, Y.; Chu, J. Stable Fluorescent NH<sub>3</sub> Sensor Based on MAPbBr3 Encapsulated by Tetrabutylammonium Cations. *J. Alloys Compd.* **2020**, 835, 155386.
- (6) Zhang, J.; Jiang, T.; Zheng, X.; Shen, C.; Cheng, X.'a. Thickness-dependent Nonlinear Optical Properties of CsPbBr<sub>3</sub> Perovskite Nanosheets. *Opt. Lett.* **2017**, 42, 3371–3374.
- (7) Li, L.; Sun, Z.; Wang, P.; Hu, W.; Wang, S.; Ji, C.; Hong, M.; Luo, J. Tailored Engineering of an Unusual  $(C_4H_9NH_3)_2(CH_3NH_3)_2Pb_3Br_{10}$  Two-Dimensional Multilayered Perovskite Ferroelectric for a High-Performance Photodetector. *Angew. Chem. Int. Ed. Engl* **2017**, *56*, 12150–12154.
- (8) Guo, D.; Bartesaghi, D.; Wei, H.; Hutter, E. M.; Huang, J.; Savenije, T. J. Photoluminescence from Radiative Surface States and Excitons in Methylammonium Lead Bromide Perovskites. *J. Phys. Chem. Lett.* **2017**, *8*, 4258–4263.
- (9) Green, M. A.; Emery, K.; Hishikawa, Y.; Warta, W.; Dunlop, E. D. Solar Cell Efficiency Tables (Version 46). *Progr. Photovolt.: Res. Appl.* **2015**, 23, 805–812.
- (10) Cui, P.; Fu, P.; Wei, D.; Li, M.; Song, D.; Yue, X.; Li, Y.; Zhang, Z.; Li, Y.; Mbengue, J. M. Reduced Surface Defects of Organometallic Perovskite by Thermal Annealing for Highly Efficient Perovskite Solar Cells. *RSC Adv.* **2015**, *5*, 75622–75629.
- (11) Song, D.; Ji, J.; Li, Y.; Li, G.; Li, M.; Wang, T.; Wei, D.; Cui, P.; He, Y.; Mbengue, J. M. Degradation of Organometallic Perovskite Solar Cells Induced by Trap States. *Appl. Phys. Lett.* **2016**, *108*, No. 093901.
- (12) Bisquert, J.; Juarez-Perez, E. J. The Causes of Degradation of Perovskite Solar Cells. *J. Phys. Chem. Lett.* **2019**, *10*, 5889–5891.
- (13) Xiao, C.; Li, Z.; Guthrey, H.; Moseley, J.; Yang, Y.; Wozny, S.; Moutinho, H.; To, B.; Berry, J. J.; Gorman, B.; Yan, Y.; Zhu, K.; Al-Jassim, M. Mechanisms of Electron-Beam-Induced Damage in Perovskite Thin Films Revealed by Cathodoluminescence Spectroscopy. *J. Phys. Chem. C* **2015**, *119*, 26904–26911.
- (14) Yang, J.; Siempelkamp, B. D.; Liu, D.; Kelly, T. L. Investigation of CH<sub>3</sub>NH<sub>3</sub>PbI<sub>3</sub> Degradation Rates and Mechanicsms in Controlled Humidity Environments Using in SItu Techniques. *ACS Nano* **2015q**, *9*, 1955–1963.
- (15) Christians, J. A.; Miranda Herrera, P. A.; Kamat, P. V. Transformation of the Excited State and Photovoltaic Efficiency of CH<sub>3</sub>NH<sub>3</sub>PbI<sub>3</sub> Perovskite upon Controlled Exposure to Humidified Air. *J. Am. Chem. Soc.* **2015**, *137*, 1530–1538.
- (16) Gao, X.; Zhang, X.; Yin, W.; Wang, H.; Hu, Y.; Zhang, Q.; Shi, Z.; Colvin, V. L.; Yu, W. W.; Zhang, Y. Ruddlesden-Popper Perovskites: Synthesis and Optical Properties for Optoelectronic Applications. *Adv Sci* **2019**, *6*, 1900941.

- (17) Schmidt, L. C.; Pertegas, A.; Gonzalez-Carrero, S.; Malinkiewicz, O.; Agouram, S.; Minguez Espallargas, G.; Bolink, H. J.; Galian, R. E.; Perez-Prieto, J. Nontemplate Synthesis of CH<sub>3</sub>NH<sub>3</sub>PbBr<sub>3</sub> Perovskite Nanoparticles. *J. Am. Chem. Soc.* **2014**, *136*, 850–853.
- (18) Zhang, W.; Peng, L.; Liu, J.; Tang, A.; Hu, J.-S.; Yao, J.; Zhao, Y. S. Controlling the Cavity Structures of Two-Photon-Pumped Perovskite Microlasers. *Adv. Mater.* **2016**, 28, 4040–4046.
- (19) Walters, G.; Haeberle, L.; Quintero-Bermudez, R.; Brodeur, J.; Kena-Cohen, S.; Sargent, E. H. Directional Light Emission from Layered Metal Halide Perovskite Crystals. *J. Phys. Chem. Lett.* **2020**, *11*, 3458–3465.
- (20) Vashishtha, P.; Ng, M.; Shivarudraiah, S. B.; Halpert, J. E. High Efficiency Blue and Green Light-Emitting Diodes Using Ruddlesden—Popper Inorganic Mixed Halide Perovskites with Butylammonium Interlayers. *Chem. Mater.* **2019**, *31*, 83–89.
- (21) Walters, G.; Sutherland, B. R.; Hoogland, S.; Shi, D.; Comin, R.; Sellan, D. P.; Bakr, O. M.; Sargent, E. H. Two-Photon Absorption in Organometallic Bromide Perovskites. *ACS Nano* **2015**, *9*, 9340–9346.
- (22) Chang, Y.-H.; Lin, J.-C.; Chen, Y.-C.; Kuo, T.-R.; Wang, D.-Y. Facile Synthesis of Two-dimensional Ruddlesden-Popper Perovskite Quantum Dots with Fine-tunable Optical Properties. *Nanoscale Res. Lett.* **2018**, *13*, 247.
- (23) Qin, Z.; Dai, S.; Gajjela, C. C.; Wang, C.; Hadjiev, V. G.; Yang, G.; Li, J.; Zhong, X.; Tang, Z.; Yao, Y.; Guloy, A. M.; Reddy, R.; Mayerich, D.; Deng, L.; Yu, Q.; Feng, G.; Calderon, H. A.; Robles Hernandez, F. C.; Wang, Z. M.; Bao, J. Spontaneous Formation of 2D/3D Heterostructures on the Edges of 2D Ruddlesden–Popper Hybrid Perovskite Crystals. *Chem. Mater.* 2020, 32, 5009–5015.
- (24) Gan, Z.; Cheng, Y.; Chen, W.; Loh, K. P.; Jia, B.; Wen, X. Photophysics of 2D Organic-Inorganic Hybrid Lead Halide Perovskites: Progress, Debates, and Challenges. *Adv. Sci.* **2021**, *8*, 2001843.
- (25) Maczka, M.; Zaręba, J. K.; Gagor, A.; Stefańska, D.; Ptak, M.; Roleder, K.; Kajewski, D.; Soszyński, A.; Fedoruk, K.; Sieradzki, A. [Methylhydrazinium]<sub>2</sub>PbBr<sub>4</sub>, a Ferroelectric Hybrid Organic—Inorganic Perovskite with Multiple Nonlinear Optical Outputs. *Chem. Mater.* **2021**, 33, 2331–2342.
- (26) Chen, Z.; Zhang, Q.; Zhu, M.; Chen, H.; Wang, X.; Xiao, S.; Loh, K. P.; Eda, G.; Meng, J.; He, J. In-Plane Anisotropic Nonlinear Optical Properties of Two-Dimensional Organic-Inorganic Hybrid Perovskite. *J. Phys. Chem. Lett.* **2021**, *12*, 7010–7018.
- (27) Abdelwahab, I.; Grinblat, G.; Leng, K.; Li, Y.; Chi, X.; Rusydi, A.; Maier, S. A.; Loh, K. P. Highly Enhanced Third-Harmonic Generation in 2D Perovskites at Excitonic Resonances. *ACS Nano* **2018**, *12*, 644–650.
- (28) Johnson, J. C.; Li, Z.; Ndione, P. F.; Zhu, K. Third-order Nonlinear Optical Properties of Methylammonium Lead Halide Perovskite Films. *J. Mater. Chem. C* **2016**, *4*, 4847–4852.
- (29) Ren, K.; Huang, L.; Yue, S.; Lu, S.; Liu, K.; Azam, M.; Wang, Z.; Wei, Z.; Qu, S.; Wang, Z. Turning a Disadvantage into an Advantage: Synthesizing High-quality Organometallic Halide Perovskite Nanosheet Arrays for Humidity Sensors. *J. Mater. Chem. C* **2017**, 5, 2504–2508.
- (30) Mannodi-Kanakkithodi, A.; Park, J.-S.; Martinson, A. B. F.; Chan, M. K. Y. Defect Energetics in Pseudo-Cubic Mixed Halide Lead Perovskites from First-Principles. *The Journal of Physical Chemistry C* **2020**, *124*, 16729–16738.
- (31) Meggiolaro, D.; Motti, S. G.; Mosconi, E.; Barker, A. J.; Ball, J.; Andrea Riccardo Perini, C.; Deschler, F.; Petrozza, A.; De Angelis, F. Iodine Chemistry Determines the Defect Tolerance of Lead-halide Perovskites. *Energy Environ. Sci.* **2018**, *11*, 702–713.
- (32) Motti, S. G.; Meggiolaro, D.; Martani, S.; Sorrentino, R.; Barker, A. J.; De Angelis, F.; Petrozza, A. Defect Activity in Lead Halide Perovskites. *Adv. Mater.* **2019**, *31*, 1901183.
- (33) Shi, T.; Yin, W.-J.; Hong, F.; Zhu, K.; Yan, Y. Unipolar Self-doping Behavior in Perovskite CH<sub>3</sub>NH<sub>3</sub>PbBr<sub>3</sub>. *Appl. Phys. Lett.* **2015**, *106*, 103902.

- (34) Kadys, A.; Sudzius, M.; Jarasiunas, K.; Mao, L.; Sun, N. Nondestructive Evaluation of Differently Doped InP Wafers by Timeresolved Four-wave Mixing Technique. *Mater. Sci. Eng., B* **2006**, *133*, 136–140.
- (35) Ma, G.; Tang, S. H.; Shen, J.; Zhang, Z.; Hua, Z. Defect-mode Dependence of Two-photon-absorption Enhancement in a One-dimensional Photonic Bandgap Structure. *Opt. Lett.* **2004**, *29*, 1769–1771.
- (36) Wang, R.; Ahmed, I.; Raza, F.; Li, C.; Zhang, Y. Light Slowing and All-optical Time Division Multiplexing of Hybrid Four-wave Mixing Signal in Nitrogen-vacancy Center. *Chin. Phys. B* **2020**, *29*, No. 054204.
- (37) Lenef, A.; Brown, S. W.; Redman, D. A.; Rand, S. C.; Shigley, J.; Fritsch, E. Electronic Structure of N-V Center in Diamond: Experiments. *Phys. Rev. B* **1996**, *53*, 13427–13440.
- (38) Yildirim, M.; March, S.; Mathew, R.; Gamouras, A.; Liu, X.; Dobrowolska, M.; Furdyna, J. K.; Hall, K. C. Electronic Structure of Ga<sub>1-x</sub>Mn<sub>x</sub>As Probed by Four-wave Mixing Spectroscopy. *Phys. Rev. B* **2011**, *84*, 121202.
- (39) Fassl, P.; Zakharko, Y.; Falk, L. M.; Goetz, K. P.; Paulus, F.; Taylor, A. D.; Zaumseil, J.; Vaynzof, Y. Effect of Density of Surface Defects on Photoluminescence Properties in MAPbI<sub>3</sub> Perovskite Films. *I. Mater. Chem. C* **2019**, *7*, 5285–5292.
- (40) Haris, M. P. U.; Bakthavatsalam, R.; Shaikh, S.; Kore, B. P.; Moghe, D.; Gonnade, R. G.; Sarma, D. D.; Kabra, D.; Kundu, J. Synthetic Control on Structure/Dimensionality and Photophysical Properties of Low Dimensional Organic Lead Bromide Perovskite. *Inorg. Chem.* **2018**, *57*, 13443–13452.
- (41) Kim, J.; Lee, S. H.; Lee, J. H.; Hong, K. H. The Role of Intrinsic Defects in Methylammonium Lead Iodide Perovskite. *J. Phys. Chem. Lett.* **2014**, *5*, 1312–1317.
- (42) Manser, J. S.; Kamat, P. V. Band Filling with Free Charge Carriers in Organometal Halide Perovskites. *Nat. Photonics* **2014**, *8*, 737–743
- (43) Musiienko, A.; Moravec, P.; Grill, R.; Praus, P.; Vasylchenko, I.; Pekarek, J.; Tisdale, J.; Ridzonova, K.; Belas, E.; Landová, L.; Hu, B.; Lukosi, E.; Ahmadi, M. Deep Levels, Charge Transport and Mixed Conductivity in Organometallic Halide Perovskites. *Energy Environ. Sci.* 2019, 12, 1413–1425.
- (44) Sheikh, T.; Nag, A. Mn Doping in Centimeter-Sized Layered 2D Butylammonium Lead Bromide (BA<sub>2</sub>PbBr<sub>4</sub>) Single Crystals and Their Optical Properties. *The Journal of Physical Chemistry C* **2019**, 123, 9420–9427.
- (45) Walsh, A.; Scanlon, D. O.; Chen, S.; Gong, X. G.; Wei, S. H. Self-regulation Mechanism for Charged Point Defects in Hybrid Halide Perovskites. *Angew Chem Int Ed Engl* **2015**, *54*, 1791–1794.
- (46) Yin, J.; Yang, H.; Song, K.; El-Zohry, A. M.; Han, Y.; Bakr, O. M.; Bredas, J. L.; Mohammed, O. F. Point Defects and Green Emission in Zero-Dimensional Perovskites. *J. Phys. Chem. Lett.* **2018**, *9*, 5490–5495.
- (47) Ding, J.; Lian, Z.; Li, Y.; Wang, S.; Yan, Q. The Role of Surface Defects in Photoluminescence and Decay Dynamics of High-Quality Perovskite MAPbI<sub>3</sub> Single Crystals. *J. Phys. Chem. Lett.* **2018**, *9*, 4221–4226.
- (48) Bao, J.; Zimmler, M. A.; Capasso, F.; Wang, X.; Ren, Z. F. Broadband ZnO Single-Nanowire Light-Emitting Diode. *Nano Lett.* **2006**, *6*, 1719–1722.
- (49) Koida, T.; Chichibu, S. F.; Uedono, A.; Tsukazaki, A.; Kawasaki, M.; Sota, T.; Segawa, Y.; Koinuma, H. Correlation between the Photoluminescence Lifetime and Defect Density in Bulk and Epitaxial ZnO. *Appl. Phys. Lett.* **2003**, 82, 532–534.
- (50) Hartmann, N. F.; Velizhanin, K. A.; Haroz, E. H.; Kim, M.; Ma, X.; Wang, Y.; Htoon, H.; Doorn, S. K. Photoluminescence Dynamics of Aryl sp<sup>3</sup> Defect States in Single-Walled Carbon Nanotubes. *ACS Nano* **2016**, *10*, 8355–8365.
- (51) Kang, S.; Koo, J.-J.; Seo, H.; Truong, Q. T.; Park, J. B.; Park, S. C.; Jung, Y.; Cho, S.-P.; Nam, K. T.; Kim, Z. H.; Hong, B. H. Defectengineered MoS<sub>2</sub> with Extended Photoluminescence Lifetime for

- High-performance Hydrogen Evolution. J. Mater. Chem. C 2019, 7, 10173–10178.
- (52) Qian, Q.; Peng, L.; Perea-Lopez, N.; Fujisawa, K.; Zhang, K.; Zhang, X.; Choudhury, T. H.; Redwing, J. M.; Terrones, M.; Ma, X.; Huang, S. Defect Creation in WSe<sub>2</sub> with a Microsecond Photoluminescence Lifetime by Focused Ion Beam Irradiation. *Nanoscale* **2020**, *12*, 2047–2056.
- (53) Gallart, M.; Ziegler, M.; Crégut, O.; Feltin, E.; Carlin, J. F.; Butté, R.; Grandjean, N.; Hönerlage, B.; Gilliot, P.; Gilliot, P. Determining the Nature of Excitonic Dephasing in High-quality GaN/AlGaN Quantum Wells through Time-resolved and Spectrally Resolved Four-wave Mixing Spectroscopy. *Phys. Rev. B* **2017**, *96*, No. 041303.
- (54) March, S. A.; Clegg, C.; Riley, D. B.; Webber, D.; Hill, I. G.; Hall, K. C. Simultaneous Observation of Free and Defect-bound Excitons in CH<sub>3</sub>NH<sub>3</sub>PbI<sub>3</sub> Using Four-wave Mixing Spectroscopy. *Sci. Rep.* **2016**, *6*, 39139.
- (55) March, S. A.; Riley, D. B.; Clegg, C.; Webber, D.; Liu, X.; Dobrowolska, M.; Furdyna, J. K.; Hill, I. G.; Hall, K. C. Four-Wave Mixing in Perovskite Photovoltaic Materials Reveals Long Dephasing Times and Weaker Many-Body Interactions than GaAs. *ACS Photonics* **2017**, *4*, 1515–1521.
- (56) Ko, B. A.; Sokolov, A. V.; Scully, M. O.; Zhang, Z.; Lee, H. W. H. Enhanced Four-wave Mixing Process near the Excitonic Resonances of Bulk MoS<sub>2</sub>. *Photonics Res.* **2019**, *7*, 251–259.
- (57) Marks, D. L.; Vinegoni, C.; Bredfeldt, J. S.; Boppart, S. A. Interferometric Differentiation Between Resonant Coherent Anti-Stokes Raman Scattering and Nonresonant Four-wave-mixing Processes. *Appl. Phys. Lett.* **2004**, *85*, 5787–5789.
- (58) Shen, Y.; Voronine, D. V.; Sokolov, A. V.; Scully, M. O. A Versatile Setup Using Femtosecond Adaptive Spectroscopic Techniques for Coherent Anti-Stokes Raman Scattering. *Rev Sci Instrum* **2015**, *86*, No. 083107.
- (59) Zázvorka, J.; Hlídek, P.; Grill, R.; Franc, J.; Belas, E. Photoluminescence of CdTe:In the Spectral Range around 11 eV. J. Lumin. 2016, 177, 71–81.
- (60) Pandey, J.; Soni, A. Unraveling Biexciton and Excitonic Excited States from Defect Bound States in Monolayer MoS<sub>2</sub>. *Appl. Surf. Sci.* **2019**, 463, 52–57.
- (61) Hannes, W. R.; Trautmann, A.; Stein, M.; Schäfer, F.; Koch, M.; Meier, T. Strongly Nonresonant Four-wave Mixing in Semi-conductors. *Phys. Rev. B* **2020**, *101*, No. 075203.
- (62) Draguta, S.; Thakur, S.; Morozov, Y. V.; Wang, Y.; Manser, J. S.; Kamat, P. V.; Kuno, M. Spatially Non-uniform Trap State Densities in Solution-Processed Hybrid Perovskite Thin Films. *J. Phys. Chem. Lett.* **2016**, *7*, 715–721.
- (63) deQuilettes, D. W.; Vorpahl, S. M.; Stranks, S. D.; Nagaoka, H.; Eperon, G. E.; Ziffer, M. E.; Snaith, H. J.; Ginger, D. S. Impact of Microstructure on Local Carrier Lifetime in Perovskite Solar Cells. *Science* **2015**, *348*, 683–686.
- (64) Gan, Z.; Wen, X.; Chen, W.; Zhou, C.; Yang, S.; Cao, G.; Ghiggino, K. P.; Zhang, H.; Jia, B. The Dominant Energy Transport Pathway in Halide Perovskites: Photon Recycling or Carrier Diffusion? *Adv. Energy Mater.* **2019**, *9*, 1900185.
- (65) Yamada, T.; Yamada, Y.; Nakaike, Y.; Wakamiya, A.; Kanemitsu, Y. Photon Emission and Reabsorption Processes in CH<sub>3</sub>NH<sub>3</sub>PbBr<sub>3</sub> Single Crystals Revealed by Time-Resolved Two-Photon-Excitation Photoluminescence Microscopy. *Phys. Rev. Appl.* **2017**, *7*, No. 014001.
- (66) Diab, H.; Arnold, C.; Ledee, F.; Trippe-Allard, G.; Delport, G.; Vilar, C.; Bretenaker, F.; Barjon, J.; Lauret, J. S.; Deleporte, E.; Garrot, D. Impact of Reabsorption on the Emission Spectra and Recombination Dynamics of Hybrid Perovskite Single Crystals. *J. Phys. Chem. Lett.* **2017**, *8*, 2977–2983.
- (67) Crothers, T. W.; Milot, R. L.; Patel, J. B.; Parrott, E. S.; Schlipf, J.; Muller-Buschbaum, P.; Johnston, M. B.; Herz, L. M. Photon Reabsorption Masks Intrinsic Bimolecular Charge-Carrier Recombination in CH<sub>3</sub>NH<sub>3</sub>PbI<sub>3</sub> Perovskite. *Nano Lett.* **2017**, *17*, 5782–5789.

I

- (68) Dong, N.; Li, Y.; Zhang, S.; McEvoy, N.; Gatensby, R.; Duesberg, G. S.; Wang, J. Saturation of Two-Photon Absorption in Layered Transition Metal Dichalcogenides: Experiment and Theory. *ACS Photonics* **2018**, *5*, 1558–1565.
- (69) Chen, S.; Wen, X.; Huang, S.; Huang, F.; Cheng, Y.-B.; Green, M.; Ho-Baillie, A. Light Illumination Induced Photoluminescence Enhancement and Quenching in Lead Halide Perovskite. *Solar RRL* **2017**, *1*, 160001.
- (70) Tollerud, J. O.; Cundiff, S. T.; Davis, J. A. Revealing and Characterizing Dark Excitons through Coherent Multidimensional Spectroscopy. *Phys. Rev. Lett.* **2016**, *117*, No. 097401.
- (71) Deretzis, I.; Smecca, E.; Mannino, G.; La Magna, A.; Miyasaka, T.; Alberti, A. Stability and Degradation in Hybrid Perovskites: Is the Glass Half-Empty or Half-Full? *J. Phys. Chem. Lett.* **2018**, *9*, 3000–3007
- (72) Leijtens, T.; Hoke, E. T.; Grancini, G.; Slotcavage, D. J.; Eperon, G. E.; Ball, J. M.; De Bastiani, M.; Bowring, A. R.; Martino, N.; Wojciechowski, K.; McGehee, M. D.; Snaith, H. J.; Petrozza, A. Mapping Electric Field-Induced Switchable Poling and Structural Degradation in Hybrid Lead Halide Perovskite Thin Films. *Adv. Energy Mater.* **2015**, *5*, 1500962.
- (73) Wei, Y.; Audebert, P.; Galmiche, L.; Lauret, J. S.; Deleporte, E. Photostability of 2D Organic-Inorganic Hybrid Perovskites. *Materials* **2014**, *7*, 4789–4802.
- (74) Schlipf, J.; Biessmann, L.; Oesinghaus, L.; Berger, E.; Metwalli, E.; Lercher, J. A.; Porcar, L.; Muller-Buschbaum, P. In Situ Monitoring the Uptake of Moisture into Hybrid Perovskite Thin Films. J. Phys. Chem. Lett. 2018, 9, 2015–2021.